



CHORUS

This is the accepted manuscript made available via CHORUS. The article has been published as:

Rotomagnetic coupling in fine-grained multiferroic BiFeO_3 : Theory and experiment

Anna N. Morozovska, Eugene A. Eliseev, Maya D. Glinchuk, Olena M. Fesenko, Vladimir V. Shvartsman, Venkatraman Gopalan, Maxim V. Silibin, and Dmitry V. Karpinsky

Phys. Rev. B **97**, 134115 — Published 27 April 2018

DOI: [10.1103/PhysRevB.97.134115](https://doi.org/10.1103/PhysRevB.97.134115)

**ROTOMAGNETIC COUPLING IN FINE-GRAINED MULTIFERROIC BiFeO₃:
THEORY AND EXPERIMENT**

Anna N. Morozovska^{1,*}, Eugene A. Eliseev², Maya D. Glinchuk², Olena M. Fesenko¹, Vladimir V. Shvartsman³, Venkatraman Gopalan⁴, Maxim V. Silibin^{5,6†}, and Dmitry V. Karpinsky^{7‡}

¹ *Institute of Physics, National Academy of Sciences of Ukraine,
46, pr. Nauky, 03028 Kyiv, Ukraine*

² *Institute for Problems of Materials Science, National Academy of Sciences of Ukraine,
Krjijanovskogo 3, 03142 Kyiv, Ukraine*

³ *Institute for Material Science and Center for Nanointegration Duisburg-Essen (CENIDE),
University of Duisburg-Essen, Universitätsstraße 15, 45141 Essen, Germany*

⁴ *Department of Materials Science and Engineering, Pennsylvania State University, University Park,
PA 16802, USA*

⁵ *National Research University of Electronic Technology “MIET”,
Moscow, Zelenograd, Russia*

⁶ *Institute for Bionic Technologies and Engineering I.M. Sechenov First Moscow State Medical University, 2-4
Bolshaya Pirogovskaya st., Moscow, Russia, 119991*

⁷ *Scientific-Practical Materials Research Centre of NAS of Belarus, Minsk, Belarus*

Abstract

Using Landau-Ginzburg-Devonshire (LGD) theory for BiFeO₃ dense fine-grained ceramics with quasi-spherical grains and nanosized inter-grain spaces enriched by elastic defects, we calculated a surprisingly strong size-induced increase of the antiferromagnetic transition temperature caused by the joint action of rotomagnetic and magnetostrictive coupling. Notably, all parameters included in the LGD functional have been extracted from experiments, not assumed. Complementary we performed experiments for dense BiFeO₃ ceramics, which revealed that the shift of antiferromagnetic transition to $T_N \sim 690$ K instead of $T_N \sim 645$ K for a single crystal. To explain theoretically the result, we consider the possibility to control antiferromagnetic state of multiferroic BiFeO₃ via biquadratic antiferrodistortive rotomagnetic, rotoelectric, magnetoelectric, and magnetostrictive couplings. According to our calculations the highest is the rotostriction contribution, while the magnetostrictive and electrostriction contributions appear smaller.

* Corresponding author: anna.n.morozovska@gmail.com

† Corresponding author: sil_m@mail.ru

‡ Corresponding author: dmitry.karpinsky@gmail.com

I. INTRODUCTION

Multiferroics, defined as materials with more than one ferroic long-range orders, are ideal systems for fundamental studies of couplings among the order parameters of different nature, e.g. ferroelectric (**FE**) polarization, structural antiferrodistortion (**AFD**), ferromagnetic (**FM**) and antiferromagnetic (**AFM**) order parameters [1, 2, 3, 4, 5, 6, 7, 8].

The AFD, FE, FM, and AFM degrees of freedom in multiferroics are interlinked via different types of biquadratic couplings leading to versatile phase diagrams and domain structure evolution [1-8]. The biquadratic couplings are universal for all AFD multiferroics [9]. Among them of particular interest are the "rotoelectric" Houchmandazeh-Laizerowicz-Salje coupling, that is the biquadratic coupling between the AFD order parameter and polarization [10, 11, 12], and the "direct" rotomagnetic coupling that is the biquadratic coupling between the AFD and AFM (or FM) orders [13].

Among the couplings, the rotomagnetic coupling impact is the most poorly studied both experimentally and theoretically, except experiments of Bussmann-Holder et al. [14, 15] revealed a magnetic field impact on AFD tilts in EuTiO_3 . The goal of the present work is to study theoretically the impact of rotomagnetic and rotoelectric couplings on the AFM order of multiferroic bismuth ferrite BiFeO_3 (**BFO**).

BFO is the unique multiferroic [16, 17] with a strong ferroelectric polarization and antiferromagnetism at room temperature, as well as conduction and magnetotransport on domain walls [18, 19, 20, 21]. The pronounced multiferroic properties and unusual domain structure evolution maintain in BFO thin films and heterostructures [22, 23, 24, 25, 26, 27]. Bulk BFO exhibits AFD order at temperatures below 1200 K; it is FE with a large spontaneous polarization below 1100 K and is AFM below Neel temperature $T_N \approx 650$ K [8, 28]. Recently, a complete phase diagram of BFO including the AFM, FE, and AFD phases was calculated within Landau-Ginzburg-Devonshire (**LGD**) theory [29], however the role of the rotomagnetic and rotoelectric couplings was omitted.

This work uses LGD-theory to establish the rotomagnetic coupling influence on the AFM transition temperature of BFO ceramics with quasi-spherical micron sized grains (treated as a core) and nanosized inter-grain spaces (treated as a shell). Notably, all parameters included in the LGD functional have been extracted from experiments only, and not supposed.. We also present experimental results for dense BFO ceramics, which reveal a shift of the AFM transition to $T_N \sim 690$ K instead of $T_N \sim 645$ K for a single crystal, and perform theoretical estimates of possible contributions to the shift. According to the estimates the highest contribution is due to the rotomagnetic coupling, the magnetoelectric and rotoelectric ones are smaller and much smaller, respectively.

The paper is organized as follows. The impact of the rotomagnetic and other couplings on the AFM transition of BFO is presented in Section II. Experimental results are analyzed in Section III.

Section IV is devoted to discussion of agreement between theory and experiment. Section V presents conclusions.

II. THEORETICAL DESCRIPTION

The rotomagnetic coupling is described by the term $(\xi_{ijkl}^M M_i M_j + \xi_{ijkl}^L L_i L_j) \Phi_k \Phi_l$, where M_i is ferromagnetic order parameter and L_i is the antiferromagnetic order parameter, ξ_{ijkl}^M and ξ_{ijkl}^L are rotomagnetic tensor components. The rotoelectric coupling is described by the term $\xi_{ijkl} P_i P_j \Phi_k \Phi_l$, where ξ_{ijkl} is the rotoelectric coupling coefficient, P_i is the spontaneous polarization, Φ_i are the spontaneous oxygen octahedra tilt angles [9]. The biquadratic magnetoelectric coupling is the coupling between polarization and magnetization, that is described by the term $\eta_{ijkl} P_i P_j M_k M_l$, where η_{ijkl} is the biquadratic magnetoelectric coupling coefficient and M_i is the spontaneous magnetization.

Thermodynamic potential of LGD-type that describes AFM, FE and AFD properties of BFO, including the rotomagnetic, rotoelectric and magnetoelectric biquadratic couplings includes the AFD, FE, AFM contributions and the coupling (ΔG_{BQC}) among them [29], as well as elastic energy (ΔG_{ELS}) including electrostrictive, magnetostrictive, and rotostrictive contributions existing in a strained media:

$$\Delta G = \Delta G_{AFD} + \Delta G_{FE} + \Delta G_{AFM} + \Delta G_{BQC} + \Delta G_{ELS} \quad (1)$$

Below we are mainly interested in $R3c$ phase that has nonzero $\Phi = \Phi_1 = \Phi_2 = \Phi_3$ and $P = P_1 = P_2 = P_3$ and the G-type (cycloidal) dimensionless AFM order parameter L , existing below Neel temperature. The AFD energy in the $R3c$ phase is a six-order expansion on the oxygen tilt Φ_i and its gradients,

$$\Delta G_{AFD} = a_i^{(\Phi)} \Phi_i^2 + a_{ij}^{(\Phi)} \Phi_i^2 \Phi_j^2 + a_{ijk}^{(\Phi)} \Phi_i^2 \Phi_j^2 \Phi_k^2 + g_{ijkl}^{(\Phi)} \frac{\partial \Phi_i}{\partial x_k} \frac{\partial \Phi_j}{\partial x_l} \quad (2)$$

Here Φ_i are components of pseudovectors, determining out-of-phase static rotations of oxygen octahedral groups (eigenvectors of AFD modes of lattice vibrations), and Einstein summation convention is employed.

The FE energy, ΔG_{FE} , is a six-order expansion on the polarization vector P_i and its gradients,

$$\Delta G_{FE} = a_i^{(P)} P_i^2 + a_{ij}^{(P)} P_i^2 P_j^2 + a_{ijk}^{(P)} P_i^2 P_j^2 P_k^2 + g_{ijkl}^{(P)} \frac{\partial P_i}{\partial x_k} \frac{\partial P_j}{\partial x_l}. \quad (3)$$

The AFM energy, ΔG_{AFM} , is a fourth-order expansion in terms of the AFM order parameter vector L_i , because this phase transition in BiFeO₃ is known to be the second order one, its gradient and gradient-related Lifshitz invariant [30, 31, 32].

$$\Delta G_{AFM} = a_i^{(L)} L_i^2 + a_{ij}^{(L)} L_i^2 L_j^2 + g_{ijkl}^{(L)} \frac{\partial L_i}{\partial x_k} \frac{\partial L_j}{\partial x_l} + h_{ijkl}^{(L)} P_l \left(L_j \frac{\partial L_i}{\partial x_k} - L_i \frac{\partial L_j}{\partial x_k} \right). \quad (4)$$

In accordance with the classical LGD theory, we assume that the coefficients $a_i^{(\Phi)}$ and $a_k^{(P)}$ are temperature dependent according to Barrett law [33], $a_i^{(\Phi)} = \alpha_T^{(\Phi)} T_{q\Phi} (\coth(T_{q\Phi}/T) - \coth(T_{q\Phi}/T_\Phi))$ and $a_k^{(P)} = \alpha_T^{(P)} (T_{qP} \coth(T_{qP}/T) - T_C)$, where T_Φ and T_C are corresponding virtual Curie temperatures, $T_{q\Phi}$ and T_{qP} are characteristic temperatures [34]. As it was shown recently [35] similar Barrett-type expressions can be used for the AFM coefficient $a_i^L(T)$ of pure bismuth ferrite $a_i^L(T) = \alpha_T^{(L)} T_L (\coth(T_L/T) - \coth(T_L/T_N))$ with the Neel temperature $T_N = 645$ K and characteristic temperature $T_L = 550$ K [29]. The expression $L \sim \sqrt{a_i^L(T)/a_{11}}$, being valid in the isotropic approximation, describes quantitatively both the temperature dependence of the AFM order parameter measured experimentally in BiFeO₃ by neutron scattering by Fischer et al. [28] and anomalous AFM contribution to the specific heat behaviour near the Neel temperature measured experimentally [36, 37, 38]. The gradient terms in the form of Lifshitz invariant, $h_{ijkl}^{(L)} P_l \left(L_j \frac{\partial L_i}{\partial x_k} - L_i \frac{\partial L_j}{\partial x_l} \right)$, in Eq.(4) are of the so-called ‘‘flexo-type’’ (for classification see **Table I** in Ref.[39]) and are proportional to the third power of the order parameters $\sim PL \nabla L$. Their inclusion can induce an incommensurate spin modulation below the AFM transition, namely the cycloid spin order with a period about (62-64) nm [2, 8].

The AFD-FE-AFM coupling energy ΔG_{BQC} is a biquadratic form of the order parameters L_i , P_i and Φ_i (see Suppl. Mat in Ref. [29]):

$$\Delta G_{BQC} = \zeta_{ijkl} \Phi_i \Phi_j P_k P_l + \kappa_{ij} \Phi_i^2 L_j^2 + \lambda_{ij} P_i^2 L_j^2. \quad (5)$$

For a given symmetry the coupling energy in Eq. (5) includes unknown tensorial coefficients ζ_{44} , ζ_{11} , ζ_{12} in Voight notations for the AFD-FE biquadratic couplings. Below, due to the lack of experimental data, the FE-AFM and AFD-AFM rotomagnetic and biquadratic magnetoelectric coupling constants are assumed to be isotropic, $\lambda_{ij} = \lambda \delta_{ij}$ and $\kappa_{ij} = \kappa \delta_{ij}$.

The elastic energy in the $R3c$ phase is

$$\Delta G_{ELS} = -(s_{ijkl}\sigma_{ij}\sigma_{kl} + Q_{ijkl}\sigma_{ij}P_kP_l + R_{ijkl}\sigma_{ij}\Phi_k\Phi_l + Z_{ijkl}\sigma_{ij}L_kL_l). \quad (6)$$

Here s_{ijkl} are elastic compliance tensor components, Q_{ijkl} are electrostriction tensor components, R_{ijkl} are rotostriction tensor components, and Z_{ijkl} are magnetostriction tensor components. All coefficients in the thermodynamic potential (1)-(6) were extracted from experimental data in Ref.[29], except for rotostriction, electrostriction and magnetostriction ones, which were determined in this work from independent experimental data. Details are listed in **Appendix A** in Ref.[40]. So that all parameters included in the parts (1)-(6) of LGD functional are extracted from experiments, but did not change within "a reasonable range".

Let us apply the thermodynamic approach based on the free energy (1)-(6) to a fine-grained BFO ceramics, for which the grain size R varies from several tens nanometers to several microns, and the grains are separated by a stressed inter-grain shell of thickness $R_0 = (5 - 50)$ nm [see **Fig.1(a)**]. The stresses can originate from different sources, such as surface tension itself, as well as from chemical pressure in the regions enriched by e.g. oxygen vacancies and/or other defects such as Fe clusters. Below we will show that the contributions of both these sources into the total stress are additive, and, therefore, hardly separable in many cases. This statement will be approved below mathematically.

For the case of densely packed spherical grains of radius R , which equatorial cross-section is shown in **Fig.1(b)**, the ratio of the grains volume to the inter-grain space can be elementary calculated as $\frac{6}{\pi} - 1 \approx 0.91$. The ratio η_s of the core volume to the total "shell + inter-grain" volume is smaller

than 0.91, namely $\eta_s = \frac{8R^3 - (4/3)\pi(R - R_0)^3}{(4/3)\pi(R - R_0)^3} = \frac{6R^3}{\pi(R - R_0)^3} - 1$. Hence the significant part of the

ceramics with densely packed identical spherical grains should be regarded affected by the surface, as well as by the chemical pressure created by elastic defects accumulated in the grain shells and inter-grain spaces. In reality the grains are non-spherical, different in size and so packed much more densely reducing the part of the inter-grain space dramatically.

We regard the static dielectric and magnetic response of the grain boundaries being lossless. Dielectric losses at the grain boundaries can lead to the regions with strongly increased dynamic dielectric susceptibility (Maxwell-Wagner relaxation), however such an increase contributes to the real part of dielectric susceptibility and does not affect on its imaginary part in the static limit (i.e. at zero frequency of applied fields). Consideration of the shell regions with higher or smaller magnetic susceptibility may change the situation in the dynamic case (at some finite frequency of ac magnetic

field used in some experiments, sensitive to dissipative processes). However we have no reasons to include magnetic losses to describe *dc* magnetic measurements we performed in section IV.

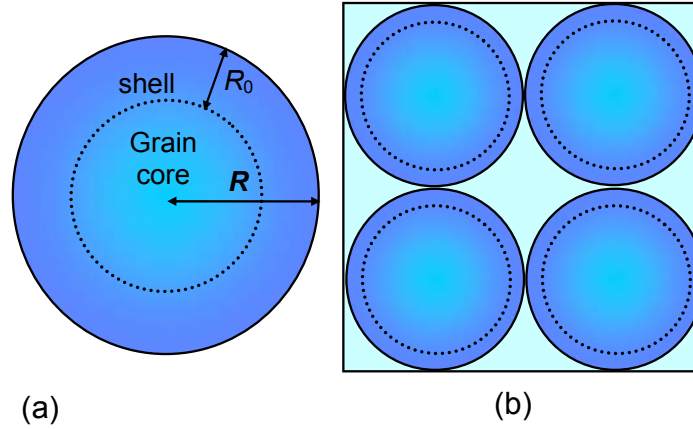


FIGURE 1. (a) Schematics of the spherical grain with radius R covered by the shell of thickness R_0 , where the stresses are accumulated. (b) Cross-section of the densely packed 8 spherical grains of radius R placed inside the cube with edge $4R$.

Therefore, for the case of the strained fine-grained ceramics Eq.(1) becomes affected by electrostrictive, rotostrictive and magnetostrictive couplings according to Eqs. (5)-(6). A formal expression for the shift of the AFM transition temperature related with the stresses near the grain boundaries can be obtained from the expression $a_j^{(L)}(T)=0$. At that the approximate formulae, $a_j^{(L)} \approx a_T^{(L)}(T - T_N) - Z_{klj}\sigma_{kl} + \kappa_{ij}\Phi_i^2 + \lambda_{ij}P_i^2$, is valid in the vicinity of Neel temperature. The expression is formal because the surface and gradient effects [42, 43, 46, 47] can contribute to the average values and their mean square deviation in a complex and a priori nontrivial way. The concrete form of the expression for $a_j^{(L)}$ depends on the physical-chemical state of the grain core and surface.

Let us limit our consideration by the most common intrinsic surface stresses [41, 42, 43,] coupled with Vegard strains (chemical pressure) [8, 44, 45] acting on both polarization \mathbf{P} , tilt Φ , and AFM order parameter \mathbf{L} via the electrostriction, rotostriction and magnetostriction couplings, respectively. Also we regard that the depolarizing field acting on ferroelectric polarization inside the grain is negligibly small due to the screening charges. Within these assumptions the radial component of the chemical pressure (denoted as $\sigma_{rr}^W(r)$) and intrinsic surface stress (denoted as $\sigma_{rr}^\mu(r)$) inside the

core and shell regions acquires the form derived in **Appendix D** [40] and Refs.[42, 43, 46, 47, 48, 49, 50], namely:

$$\sigma_{rr}^{\mu}(r) \approx \begin{cases} -\frac{\mu}{R}, & r < R - R_0, \\ -\mu \left(\frac{1}{R - R_0} - \frac{1}{R} \right), & R - R_0 < r < R. \end{cases} \quad (7a)$$

$$\sigma_{rr}^W(r) \approx \begin{cases} 0, & r < R - R_0, \\ -G \frac{1+\nu}{1-\nu} W^m \delta N_m \frac{2R^3 + r^3}{3r^3}, & R - R_0 < r < R. \end{cases} \quad (7b)$$

Here r is the distance from the grain centre. The components of intrinsic surface stress tensor are regarded diagonal, i.e. $\mu_{kl} = \mu \delta_{kl}$ and μ is about $(1 - 10)\text{N/m}$. Poisson ratio is $\nu = -s_{12}/s_{11}$ for cubic $m3m$ symmetry in the parent phase. $G = (c_{11} - c_{12})/2$ is the shear modulus.

The Vegard strain tensor W_{kl}^m of m -th type defects is regarded diagonal, $W_{kl}^m = W^m \delta_{kl}$. For perovskites ABO_3 the Vegard strain tensor is often related with vacancies and its absolute value can be estimated as $|W| \propto (5 - 30) \text{\AA}^3$ for different vacancies [45]. Note that the Vegard tensor is usually diagonal for oxygen vacancies in perovskites, but not isotropic [45]. Notably, "compositional" Vegard strains $\delta u_{kl} = W_{kl}^m \delta N_m$ can reach percents for vacancies concentration variation $\delta N_m \sim 10^{27} \text{m}^{-3}$ the near the surface. The value corresponds to approximately one defect per 10 unit cells for the typical cell concentrations in perovskites $\sim 1.5 \times 10^{28} \text{m}^{-3}$. Despite the concentration is much higher than the defect concentration in a bulk [51], such values are typical for vacancies segregation near the surface due to the strong lowering of their formation energy at the surface [52, 53].

Let us average the total stress $\sigma_{rr}(r) = \sigma_{rr}^W(r) + \sigma_{rr}^{\mu}(r)$ in Eqs.(7) over the grain volume $V = \frac{4}{3} \pi R^3$ under the condition $R_0 \ll R$. Using calculations listed in **Appendix D** [40] the averaging yields

$$\langle \sigma_{rr}(R) \rangle \approx \eta \frac{R_0}{R}, \quad \eta = -\frac{\mu}{R_0} - 3G \frac{1+\nu}{1-\nu} W^m \delta N_m. \quad (8)$$

As one can see from the explicit form of the "total stress" parameter η , its first term ($\sim \mu$) originates from the intrinsic surface stress, and the second term ($\sim W^m \delta N_m$) originates from the excess chemical pressure. Thus Eq.(8) proves that both the chemical pressure and surface tension contributes into the total stress additively, and, therefore are hardly separable in many cases.

Assuming that the coupling between the AFM and AFD, AFM and FE order parameters is weak, the decoupling approximation is valid with high accuracy, and so the renormalized AFM

transition temperature for a quasi-spherical grain of radius R covered by a thin shell of thickness R_0 acquires the form derived in **Appendix B** [40]:

$$T_{AFM} \approx T_N - \frac{1}{\alpha_T^{(L)}} \left[\frac{\kappa(2R_{12} + R_{11})}{|a_{11}^{(\Phi)}|} + \frac{\lambda(2Q_{12} + Q_{11})}{|a_{11}^{(P)}|} - (2Z_{12} + Z_{11}) \right] \eta \frac{R_0}{R}. \quad (9)$$

The shift of T_N in Eq.(9) contains three contributions, namely rotomagnetic [proportional to $\kappa(2R_{12} + R_{11})$], rotoelectric [proportional to $\lambda(2Q_{12} + Q_{11})$] and magnetostrictive [proportional to $(2Z_{12} + Z_{11})$] couplings with the total stress $\langle \sigma_{rr}(R) \rangle \sim \eta \frac{R_0}{R}$. Estimation of the contributions for the parameters from **Table I** gives for the coefficients of the rotomagnetic, rotoelectric and magnetostrictive contributions following values

$$\frac{1}{\alpha_T^{(L)}} \frac{\kappa(2R_{12} + R_{11})}{a_{11}^{(\Phi)}} \cong -1.53 \times 10^{-8} \frac{Km^3}{J}, \quad \frac{1}{\alpha_T^{(L)}} \frac{\lambda(2Q_{12} + Q_{11})}{a_{11}^{(P)}} \cong 2.19 \times 10^{-9} \frac{Km^3}{J},$$

$$\frac{2Z_{12} + Z_{11}}{\alpha_T^{(L)}} \cong -1.2 \times 10^{-8} \frac{Km^3}{J}. \quad (10)$$

The rotomagnetic and rotoelectric coupling contributions to the shift of T_N given by Eq.(9) are different in sign because the sum $2R_{12} + R_{11} = -2.18 \times 10^{18} \text{ m}^{-2}$ is negative, and sum $Q_{11} + 2Q_{12} = 0.0235 \text{ m}^4/\text{C}^2$ appears positive for BFO (see **Table I**). According to the estimates (10) the largest is the rotomagnetic contribution, the magnetostrictive one is a bit smaller, and the rotoelectric contribution is about an order of magnitude smaller.

Table I. LG potential for BiFeO₃

<i>Parameter</i>	<i>SI units</i>	<i>Value for BiFeO₃</i>	<i>Reference</i>
$a_{11}^{(\Phi)}$	J/m ⁷	$-4.53 \times 10^{49} + 4.5 \times 10^{48} \times \coth(300/T)$	[29]
$a_{11}^{(P)}$	m ⁵ J/(C ⁴)	-1.35×10^9	[29]
$a_{111}^{(\Phi)}$	J/m ⁹	$16.72 \times 10^{70} - 3.4 \times 10^{70} \times \coth(400/T)$	[29]
$a_{111}^{(P)}$	m ⁹ J/(C ⁶)	11.2×10^9	[29]
κ	J/(A ² m ³)	7.4×10^{17}	[29]
λ	J m ³ /(A ² C ²)	3.8×10^{-4}	[29]
α_{LT}	J/(A ² m K)	3.02×10^{-6}	see Appendix C
T_N	K	645	Neel temperature

β_L	J m/A ⁴	1.03×10^{-14}	see Appendix C
Q_{ij}	m ⁴ /C ²	$Q_{11} + 2Q_{12} = 0.0235$	see Appendix A
R_{ij}	m ⁻²	$2R_{12} + R_{11} = -2.18 \times 10^{18}$	see Appendix A
Z_{ij}	m ² /A ²	$Z_{11} + 2Z_{12} = 3.65 \times 10^{-14}$	see Appendix C
c_{ij}	Pa	$c_{11} = 3.02 \times 10^{11}$; $c_{12} = 1.62 \times 10^{11}$; $c_{44} = 0.68 \times 10^{11}$	[54]

Notably, the gradient terms in the form of Lifshitz invariant in Eq.(4) do not contribute to the AFM transition shift given by Eq.(9), since these terms are proportional to the third power of the order parameters $\sim PL \nabla L$, while only the second powers can contribute significantly to the transition temperature of small nanoparticles with radius less than (10 – 25) nm. The Lifshitz invariant inclusion induces the incommensurate modulation below AFM transition [30-32], which we do not consider in this work.

A physical analysis of the different contributions in Eq.(9) leads to a more comprehensive semi-microscopic explanation why T_N can be shifted in fine-grained ceramics. Actually elastic defects located in the thin shell regions create long-range elastic strain fields, which spread out to the core far beyond the grain shells, in contrast to the stress field that exist only in the shell in accordance with Eq.(7b). The strains leading to the bonds length changes, distortions and antiferrodistortive rotations via the rotostrictive, rotoelectrostrict and magnetostrictive coupling mechanisms induce to the changes of the antiferromagnetic exchange integral between electron spins (evidently via the changes of the corresponding electron wave functions overlap). Allowing for the specific signs of the coupling strength (priority due to the negative rotostrictive coupling in BFO) the elastic fields lead to the increase of T_N . Meanwhile the decrease of T_N in other antiferrodistortive-antiferromagnets, or for other shape and/or geometry of the nano-inclusions is not excluded.

We show the dependence of the AFM transition temperature T_{AFM} on the grain radius R in **Fig. 2(a)**. The rotoelectric, magnetostrictive and rotomagnetic contributions to T_{AFM} are shown in **Fig. 2(b)**.

From **Fig.2(b)** the size-induced increase of the AFM temperature is caused by the rotomagnetic and magnetostrictive couplings. The rotoelectric coupling leads to the decrease AFM transition, and the corresponding shift is several times smaller than the increase caused by the rotomagnetic coupling accordingly to the estimates (10).

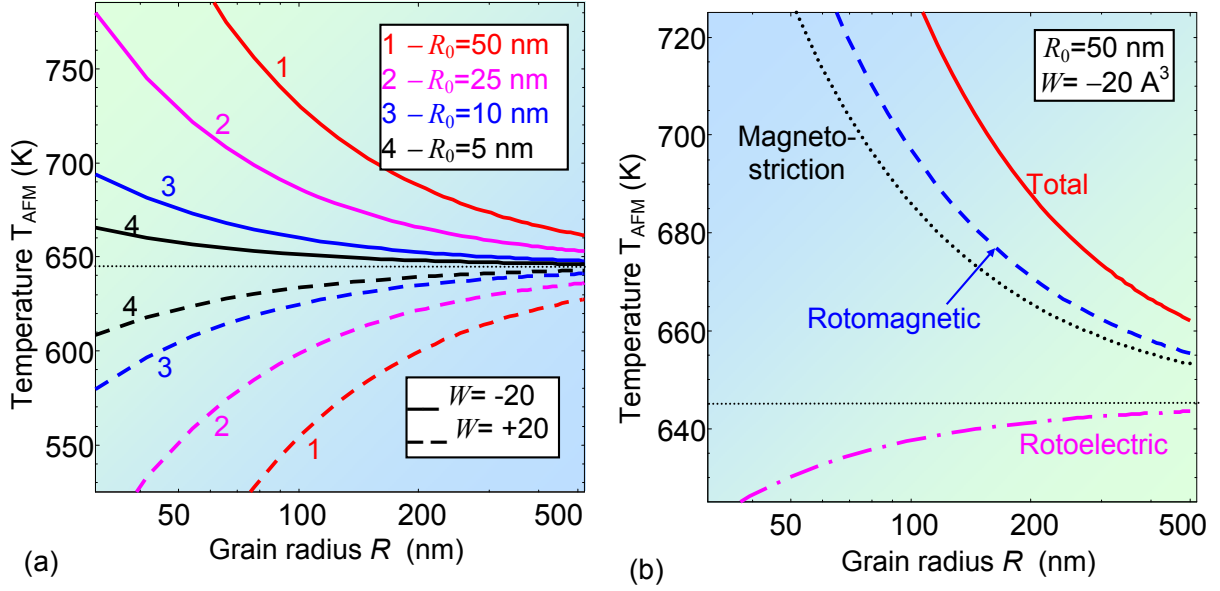


FIGURE 2. (a) Dependences of the AFM transition temperature T_{AFM} vs. the grain radius R calculated from Eq.(8) for several shell thicknesses $R_0 = 50$ nm (curves 1), $R_0 = 25$ nm (curves 2), $R_0 = 10$ nm (curves 3), and $R_0 = 5$ nm (curves 4). Total Vegard coefficient $W = \sum_m W_m$ is equal to -20 Å³ for solid curves and $+20$ Å³ for dashed curves. (b) Separate contributions (rotomagnetic, magnetostriction and rotoelectric) to the T_{AFM} . Surface tension coefficient $\mu = 5$ N/m and total defect concentration in the shell $\sum_m \delta N_m = 10^{27}$ m⁻³. Other parameters are taken from **Table 1**.

Color map of the AFM transition temperature T_{AFM} in coordinates "grain radius R – shell thickness R_0 " was calculated from Eq.(8) and is shown in **Figs.3 (a, b, c)** for the positive, zero and negative Vegard coefficient W , respectively. From the figures one can see that the positive and zero W decrease the transition temperature [see **Figs.3 (a, b)**], and only the negative W can increase it [see **Fig.3 (c)**]. The increase is significant for relatively small grains with radius less than 200 nm and thick shells with thickness more than 10 nm.

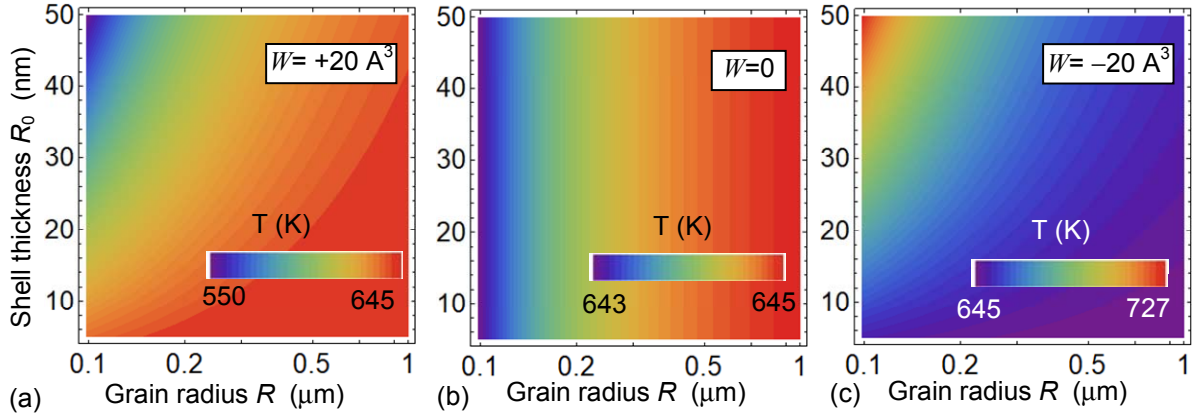


FIGURE 3. Color map of the AFM transition temperature T_{AFM} in coordinates "grain radius R – shell thickness R_0 " calculated from Eq.(9) for the same parameters as in **Fig.2** and **Table 1**.

III. EXPERIMENTAL RESULTS

A polycrystalline BFO sample prepared by a two-stage solid-state reaction technique [55] was characterized by a single phase rhombohedral structure described by $R3c$ space group [56]. The XRD data affirmed a chemical homogeneity of the compound with an accuracy of about 3%, which is conditioned by the precision of a conventional X-ray diffractometer [**Fig. 4(c)**]. The synthesis conditions used to prepare the sample, viz. quite high final sintering temperature of 880°C applied for a short time period (10 min) allowed getting the high purity compound with a typical grain size of about 1-5 μm coexisting with an intergranular texture. The compound is characterized by an increased amount of the intergranular texture, which volume fraction is about 1% as confirmed by the SEM measurements. This amount is significantly larger than the values attributed to similar compounds prepared by conventional solid state reaction technique. It is assumed that the structure of the intergranular texture is highly defective because of a numerous dislocations, inhomogeneous stress distribution and local variations of the chemical composition.

Temperature dependences of magnetization were measured in zero field cooled (ZFC) and field cooled (FC cooling) modes in the temperature range of 300 – 1000 K under magnetic field of 1kOe with a slow scan rate (2 seconds per measuring point, accuracy ~ 0.1 K). Small value of the remnant magnetization [**Figs. 4(a,b)**] is associated with the weak ferromagnetic state that becomes pronounced due to disruption of the spatially modulated magnetic structure occurred in the vicinity of numerous structural defects specific for the compound. Temperature dependent magnetization measurements allow observing the significantly shifted antiferromagnetic transition temperature ($T_N \sim 690\text{K}$) as compared to the widely noted value of 640 K specific for BFO single crystals [57, 58] [see **Fig.4(b)**]. SEM images of the dense ceramics for different magnifications are shown in **Fig.4(d)-(f)**.

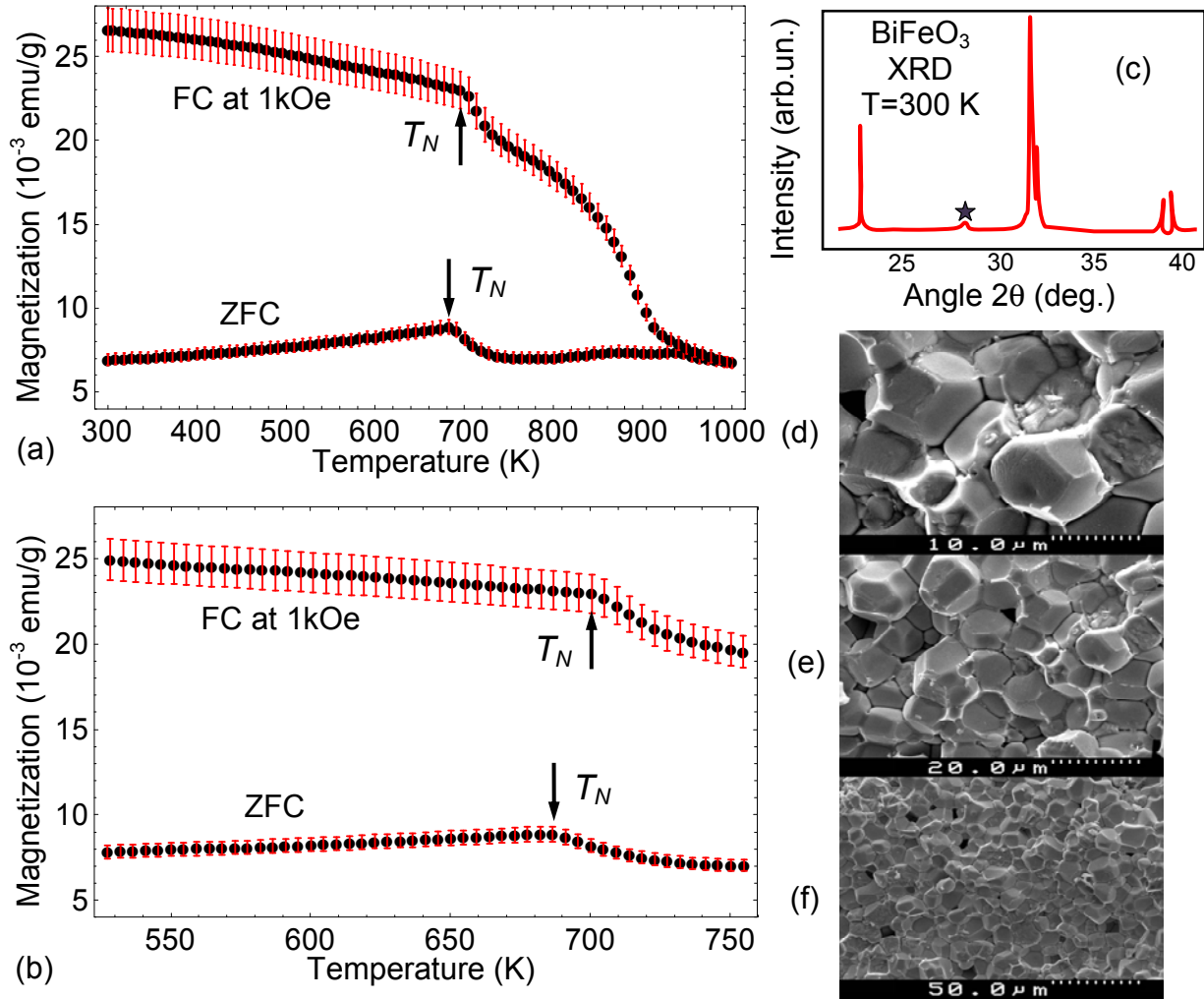


FIGURE 4. (a,b) Temperature dependences of magnetization measured in the BFO ceramics under ZFC (lower curve) and FC condition (magnetic field of 1 kOe, upper curve). Plot (b) is the part of the plot (a) in the vicinity of the AFM transition temperature. Error bars are shown by red lines. XRD data shown in the inset (c) testify the phase purity of the studied BFO ceramics (tiny amount of the Fe_2O_3 impurity phase is marked by asterisk symbol). (d)-(f) SEM images of the dense BFO ceramics for different magnifications.

It should be noted that the AFM transition temperature is shifted towards high temperatures for both FC and ZFC curves, and the difference in the magnetic anomalies observed at both magnetization dependences is about 10 K and cannot be caused by some drawbacks in the measuring procedure. The FC and ZFC curves do not merge above T_N because the magnetization data testify a presence of a magnetic impurity (viz. $\gamma\text{-Fe}_2\text{O}_3$ phase with a volume fraction of less than 1% as confirmed by the XRD measurements). The phase forms notable “background” into the magnetization curves lasting up to a temperature above 900 K, and one should note similar behavior of the temperature dependences of magnetization observed for single-crystal and ceramic BiFeO_3 [57, 59]. Assuming a negligibly small

amount of the mentioned magnetic impurity one should not consider any significant effect on the magnetic transition temperature of the compound. The increased value of the magnetic transition temperature can be explained by a joint action of the rotomagnetic and magnetostriction coupling, which are usually very small in a homogeneous bulk BFO crystal and lead to the temperature shift of about 0.5 – 5 K. These couplings can be much more pronounced in ceramics due to the internal intergranular stresses. In this sense relevant phenomenology allows some insight to the intrinsic stress and strain gradients.

IV. DISCUSSION

To relate the above theoretical estimates with the experimental results shown in **Fig.4(a, b)** we assume that several types of defects (oxygen vacancies and Fe clusters) are accumulated in the shells and their influence is synergetic. For the case the total defect concentration can reach relatively high values in the shell, $\sum_m \delta N_m = 10^{27} \text{ m}^{-3}$. In order to compare the above theory with the experimental results shown in **Fig.4(b)** the observable physical quantities (e.g. magnetization \mathbf{M}) should be averaged over the grain radius R and shell thicknesses R_0 with a definite normalized distribution function $f(R, R_0)$. Since $M^2 \sim (T - T_{AFM})$, the averaged AFM transition temperature is given by expression:

$$\langle T_{AFM} \rangle = \int_{R_{\min}}^{R_{\max}} dR \int_{R_0^{\min}}^{R_0^{\max}} dR_0 f(R, R_0) T_{AFM}(R, R_0). \quad (11)$$

For instance, assuming that the shell thickness R_0 is constant, and the distribution of grain radius is quasi-homogeneous between R_{\min} and R_{\max} , i.e. $\langle T_{AFM} \rangle = \int_{R_{\min}}^{R_{\max}} \frac{dR T_{AFM}(R, R_0)}{R_{\max} - R_{\min}}$, one obtains from

Eqs.(9)-(11) that

$$\langle T_{AFM} \rangle \approx T_N + \frac{1}{\alpha_T^{(L)}} \left[\frac{\lambda(2Q_{12} + Q_{11})}{|a_{11}^{(P)}|} + \frac{\kappa(2R_{12} + R_{11})}{|a_{11}^{(\Phi)}|} - (2Z_{12} + Z_{11}) \right] \frac{\eta}{2\Delta R} \ln \left(\frac{\langle R \rangle + \Delta R}{\langle R \rangle - \Delta R} \right) \quad (12)$$

Where $\langle R \rangle = \frac{R_{\max} + R_{\min}}{2}$, $\Delta R = \frac{R_{\max} - R_{\min}}{2}$, and $\Delta R = \langle R \rangle - R_{\min}$. In **Fig. 5** the dependence of the averaged AFM transition temperature $\langle T_{AFM} \rangle$ on R_{\max} is shown for $R_0 \approx 45 \text{ nm}$, $R_{\min} \approx 50 \text{ nm}$ and $W = -20 \text{ \AA}^3$. The values R_0 and R_{\min} where taken for illustration, they are within reasonable ranges $5 \leq R_0 \leq 50 \text{ nm}$ [47] and $50 < R_{\min} < 500 \text{ nm}$, which are typical for sub-micro and nanograind ceramics and satisfy the necessary condition $R_0 \leq R_{\min}$. According to **Fig. 5** the increase of $\langle T_{AFM} \rangle$ above 45 K is possible for the ceramic with the average grain radius below 150 nm. However according the **Fig. 5** for the ceramics with the average grain size about 5 μm the Neel temperature

should be about 650 K that is close to the single crystal value 645 K. The discrepancy between the calculated and measured Neel temperature cannot originate from the dielectric or magnetic losses, which are not considered in the proposed static model. Actually the dynamics losses can only decrease the theoretical predictions of AFM temperature and so increase the discrepancy between the theory and experiment.

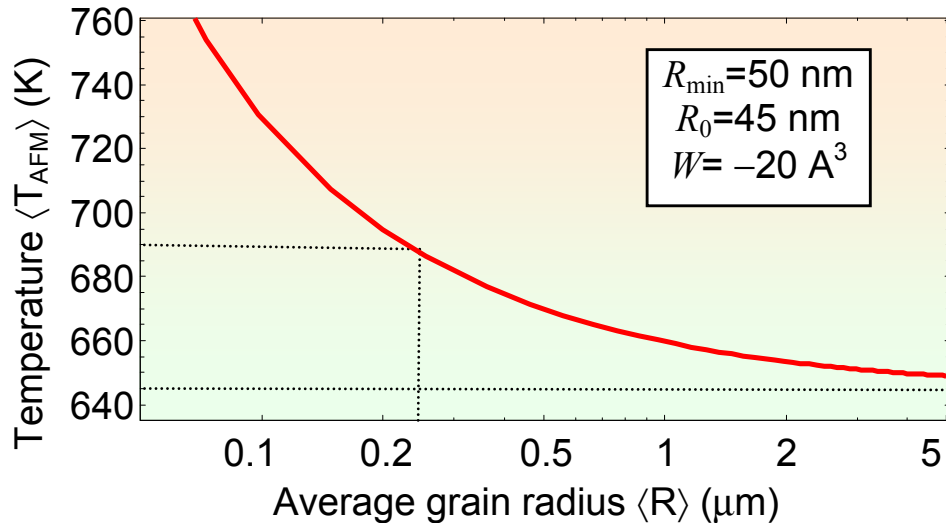


FIGURE 5. The dependence of the averaged transition temperature $\langle T_{AFM} \rangle$ on the average grain radius $\langle R \rangle$ calculated from Eq.(10) for minimal grain radius $R_{\min} \approx 50 \text{ nm}$, shell thickness $R_0 \approx 45 \text{ nm}$, and Vegard coefficient $W = -20 \text{ \AA}^3$. Other parameters are the same parameters as in **Fig.2** and **Table 1**.

Hence the proposed theoretical model can explain experimental data shown in **Fig.4(a)** only qualitatively, because it gives the increase of $\langle T_{AFM} \rangle$ above 45 K for fine-grained ceramics with significant amount of grains with radius smaller than 250 nm. The one order of magnitude discrepancy between the average grain sizes required from the theoretical model (less than 500 nm) and experiment (about 5 μm) to reach the increase of $\langle T_{AFM} \rangle$ above 45 K evidently speaks in favor of strongly underestimated impact of the rotomagnetic coupling by the model parameters or unexpectedly high contribution of the small grains into the average magnetization (non-uniform distribution function of the grain sizes).

V. SUMMARY

Using Landau-Ginzburg-Devonshire theory for BiFeO_3 dense ceramics with quasi-spherical micron sized grain cores and nanosized inter-grain spaces we calculated a surprisingly strong size-induced increase of the AFM transition temperature caused by the joint action of the rotomagnetic and

magnetostriction coupling with elastic stresses accumulated in the inter-grain spaces. The rotoelectric coupling leads to the decreasing AFM transition temperature, and the corresponding shift is several times smaller than the increase caused by the rotomagnetic coupling.

Also we performed experiments for dense BiFeO₃ ceramics, which revealed the AFM transition at $T_N \sim 690$ K instead of $T_N \sim 645$ K for a single crystal. To explain qualitatively the result we consider the possibility to control AFM properties of multiferroic BiFeO₃ via the biquadratic antiferrodistortive rotomagnetic, rotoelectric and magnetostrictive couplings. To reach quantitative agreement between the theoretical model and experimental data one could also consider low symmetry phases [60, 61] with possibly higher impact of the rotomagnetic coupling and other LG parameters.

Acknowledgments. This project (A.N.M., O.M.F. and D.V.K.) has received funding from the European Union's Horizon 2020 research and innovation programme under the Marie Skłodowska-Curie grant agreement No 778070 – TransFerr – H2020-MSCA-RISE-2017. A.N.M. work was partially supported by the National Academy of Sciences of Ukraine (projects No. 0117U002612 and No. 0118U003375). V.G. acknowledges the National Science Foundation grant number DMR-1420620. D.V.K. and M.V.S. acknowledge MK-1720.2017.8 and RFFI (# 17-58-45026)

REFERENCES

- [1] M. Fiebig, Revival of the magnetoelectric effect, *Journal of Physics D: Applied Physics* 38, R (2005).
- [2] N. A. Spaldin and M. Fiebig, The renaissance of magnetoelectric multiferroics, *Science* 309, 391 (2005).
- [3] J.M. Rondinelli and N.A. Spaldin, Structure and properties of functional oxide thin films: insights from electronic-structure calculations, *Advanced materials* 23, 3363 (2011).
- [4] A. P., Pyatakov and A. K.Zvezdin, Magnetoelectric and multiferroic media, *Physics-Uspexhi* 55, 557 (2012).
- [5] J. F. Scott, Data storage: Multiferroic memories, *Nature materials* 6, 256 (2007).
- [6] M. Fiebig, T. Lottermoser, D. Meier, and M. Trassin, The evolution of multiferroics, *Nature Reviews Materials* 1, 16046 (2016)
- [7] E.V. Balashova and A.K. Tagantsev, Polarization response of crystals with structural and ferroelectric instabilities, *Phys. Rev. B* 48, 9979 (1993).
- [8] G. Catalan and James F. Scott, Physics and applications of bismuth ferrite, *Adv. Mater.* 21, 2463 (2009).
- [9] V. Gopalan and D.B. Litvin, Rotation-reversal symmetries in crystals and handed structures, *Nature Materials* 10, 376 (2011).
- [10] M. J. Haun, E. Furman, T. R. Halemane, and L. E. Cross, Thermodynamic theory of the lead zirconate-titanate solid solution system, part IV: Tilting of the oxygen octahedra, *Ferroelectrics*, 99, 55 (1989).
- [11] A.K. Tagantsev, E. Courtens and L. Arzel, Prediction of a low-temperature ferroelectric instability in antiphase domain boundaries of strontium titanate, *Phys. Rev. B*, 64, 224107 (2001).
- [12] B. Houchmanzadeh, J. Lajzerowicz, and E Salje, Order parameter coupling and chirality of domain walls, *J. Phys.: Condens. Matter* 3, 5163 (1991)
- [13] E.A. Eliseev, M.D. Glinchuk, Venkatraman Gopalan, and A.N. Morozovska, Rotomagnetic couplings influence on the magnetic properties of antiferrodistortive antiferromagnets, *J. Appl. Phys.* 118, 144101 (2015)
- [14] Z. Guguchia, H. Keller, J. Köhler, and A. Bussmann-Holder, Magnetic field enhanced structural instability in EuTiO_3 , *J. Phys.: Condens. Matter* 24, 492201 (2012).
- [15] K. Caslin, R. K. Kremer, Z. Guguchia, H. Keller, J. Köhler, and A. Bussmann-Holder, Lattice and polarizability mediated spin activity in EuTiO_3 , *J. Phys.: Condens. Matter* 26, 022202 (2014).
- [16] D.C. Arnold, K.S. Knight, G. Catalan, S.A.T. Redfern, James F. Scott, Philip Lightfoot, and Finlay D. Morrison, The β -to- γ Transition in BiFeO_3 : A Powder Neutron Diffraction Study, *Advanced Functional Materials* 20, 2116 (2010).
- [17] R. Palai, R. S. Katiyar, Hans Schmid, Paul Tissot, S. J. Clark, Jv Robertson, S. A. T. Redfern, G. A. Catalan, and J. F. Scott, β phase and γ - β metal-insulator transition in multiferroic BiFeO_3 , *Phys. Rev. B* 77, 014110 (2008).
- [18] J. Seidel, L.W. Martin, Q. He, Q. Zhan, Y.-H. Chu, A. Rother, M. E. Hawkrige, P. Maksymovych, P. Yu, M. Gajek, N. Balke, S. V. Kalinin, S. Gemming, F. Wang, G. Catalan, J. F. Scott, N. A. Spaldin, J. Orenstein, and R. Ramesh, Conduction at domain walls in oxide multiferroics, *Nature materials* 8, 229 (2009).

-
- [19] J. Seidel, P. Maksymovych, Y. Batra, A. Katan, S.-Y. Yang, Q. He, A. P. Baddorf, S.V. Kalinin, C.-H. Yang, J.-C. Yang, Y.-H. Chu, E. K. H. Salje, H. Wormeester, M. Salmeron, and R. Ramesh, Magnetotransport at domain walls in BiFeO₃, *Phys. Rev. Lett.* 108, 067203 (2012).
- [20] Q. He, C.-H. Yeh, J.-C. Yang, G. Singh-Bhalla, C.-W. Liang, P.-W. Chiu, G. Catalan, L.W. Martin, Y.-H. Chu, J. F. Scott, and R. Ramesh, Magnetotransport at domain walls in BiFeO₃, *Phys. Rev. Lett.* 108, 067203 (2012).
- [21] G. Catalan, J. Seidel, R. Ramesh, and J. F. Scott, Domain wall nanoelectronics, *Rev. Mod. Phys.* 84, 119 (2012).
- [22] J. Wang, J. B. Neaton, H. Zheng, V. Nagarajan, S. B. Ogale, B. Liu, D. Viehland, V. Vaithyanathan, D. G. Schlom, U. V. Waghmare, N. A. Spaldin, K. M. Rabe, M. Wuttig, and R. Ramesh, Epitaxial BiFeO₃ multiferroic thin film heterostructures, *Science* 299, 1719 (2003).
- [23] Y.-H. Chu, Qian Zhan, L. W. Martin, M. P. Cruz, Pei-Ling Yang, G.W. Pabst, F. Zavaliche, Seung-Yeul Yang, Jing-Xian Zhang, Long-Qing Chen, D. G. Schlom, I.-Nan Lin, Tai-Bor Wu, and Ramamoorthy Ramesh, Nanoscale domain control in multiferroic BiFeO₃ thin films, *Advanced Materials* 18, 2307 (2006).
- [24] Ying-Hao Chu, L.W. Martin, M.B. Holcomb, M. Gajek, Shu-Jen Han, Qing He, N. Balke, Chan-Ho Yang, Donkoun Lee, Wei Hu, Qian Zhan, Pei-Ling Yang, A. Fraile-Rodríguez, A. Scholl, Shan X. Wang, and Ramamoorthy Ramesh, Electric-field control of local ferromagnetism using a magnetoelectric multiferroic, *Nature materials* 7, 478 (2008).
- [25] P. Maksymovych, M. Huijben, Minghu Pan, S. Jesse, N. Balke, Ying-Hao Chu, Hye Jung Chang, A.Y. Borisevich, A.P. Baddorf, Guus Rijnders, D.H. A. Blank, Ramamoorthy Ramesh, and S.V. Kalinin, Ultrathin limit and dead-layer effects in local polarization switching of BiFeO₃, *Phys. Rev. B*, 85, 014119 (2012).
- [26] C. Beekman, W. Siemons, M. Chi, N. Balke, J. Y. Howe, T. Z. Ward, P. Maksymovych, J. D. Budai, J. Z. Tischler, R. Xu, W. Liu, and H. M. Christen, Ferroelectric Self-Poling, Switching, and Monoclinic Domain Configuration in BiFeO₃ Thin Films, *Advanced Functional Materials* 26, 5166 (2016).
- [27] M. Trassin, G. De Luca, S. Manz, and M. Fiebig, Probing ferroelectric domain engineering in BiFeO₃ thin films by second harmonic generation, *Advanced Materials* 27, 4871 (2015).
- [28] P. Fischer, M. Polomska, I. Sosnowska, and M. Szymanski, Temperature dependence of the crystal and magnetic structures of BiFeO₃, *Journal of Physics C: Solid State Physics* 13, 1931 (1980).
- [29] D.V. Karpinsky, E.A. Eliseev, Fei Xue, M.V. Silibin, A. Franz, M.D. Glinchuk, I.O. Troyanchuk, S.A. Gavrilov, Venkatraman Gopalan, Long-Qing Chen, and A.N. Morozovska, Thermodynamic potential and phase diagram for multiferroic bismuth ferrite (BiFeO₃), *npj Computational Materials* 3, 20 (2017)
- [30] Pierre Tolédano, Pseudo-proper ferroelectricity and magnetoelectric effects in TbMnO₃, *Phys. Rev. B* 79, 094416 (2009).
- [31] A. Brooks Harris, Ferroelectricity induced by incommensurate magnetism, *J. Appl. Phys.* 99, 08E303 (2006).

-
- [32] B. Ruetter, S. Zvyagin, A.P. Pyatakov, A. Bush, J. F. Li, V. I. Belotelov, A. K. Zvezdin, and D. Viehland, Magnetic-field-induced phase transition in BiFeO₃ observed by high-field electron spin resonance: Cycloidal to homogeneous spin order, *Phys. Rev. B* 69, 064114 (2004).
- [33] J.H. Barrett, Dielectric constant in perovskite type crystals, *Phys. Rev.* 86, 118 (1952).
- [34] Yijia Gu, K.Rabe, E. Bousquet, Venkatraman Gopalan, and Long-Qing Chen, Phenomenological thermodynamic potential for CaTiO₃ single crystals, *Phys. Rev. B* 85, 064117 (2012).
- [35] A.N. Morozovska, V.V. Khist, M.D. Glinchuk, Venkatraman Gopalan, and E.A. Eliseev, Linear antiferrodistortive-antiferromagnetic effect in multiferroics: Physical manifestations, *Phys. Rev. B* 92, 054421 (2015).
- [36] J.R. Chen, W.L. Wang, J.-B. Li, G.H. Rao, X-ray diffraction analysis and specific heat capacity of (Bi_{1-x}La_x)FeO₃ perovskites, *Journal of Alloys and Compounds* 459, 66 (2008).
- [37] S. N. Kallaev, Z. M. Omarov, R. G. Mitarov, A. R. Bilalov, G. G. Gadzhiev, L. A. Reznichenko, R. M. Ferzilaev, S. A. Sadykov, Heat Capacity and Dielectric Properties of Multiferroics Bi_{1-x}Gd_xFeO₃ (x = 0–0.20), *Physics of the Solid State* 56, 1412 (2014).
- [38] A. A. Amirov, A. B. Batdalov, S. N. Kallaev, Z. M. Omarov, I. A. Verbenko, O. N. Razumovskaya, L. A. Reznichenko, and L. A. Shilkina, Specific features of the thermal, magnetic, and dielectric properties of multiferroics BiFeO₃ and Bi_{0.95}La_{0.05}FeO₃, *Physics of the Solid State* 51, 1189 (2009).
- [39] E.A. Eliseev, S.V. Kalinin, Yijia Gu, M. D. Glinchuk, V.V. Khist, A. Borisevich, Venkatraman Gopalan, Long-Qing Chen, and A. N. Morozovska, Universal emergence of spatially modulated structures induced by flexoantiferrodistortive coupling in multiferroics, *Phys. Rev. B* 88, 224105 (2013).
- [40] Supplementary Materials, URL will be provided by Publisher
- [41] V.A. Shchukin and D. Bimberg, Spontaneous ordering of nanostructures on crystal surfaces, *Rev. Mod. Phys.* 71, 1125 (1999).
- [42] A.N. Morozovska, E.A. Eliseev, and M.D. Glinchuk, Ferroelectricity enhancement in confined nanorods: Direct variational method, *Phys. Rev. B* 73, 214106 (2006).
- [43] A. N. Morozovska, M. D. Glinchuk, and E.A. Eliseev, Phase transitions induced by confinement of ferroic nanoparticles, *Phys. Rev. B* 76, 014102 (2007).
- [44] X. Zhang, A. M. Sastry, W. Shyy, Intercalation-induced stress and heat generation within single lithium-ion battery cathode particles, *J. Electrochem. Soc.* 155, A542 (2008).
- [45] D.A. Freedman, D. Roundy, and T. A. Arias, Elastic effects of vacancies in strontium titanate: Short-and long-range strain fields, elastic dipole tensors, and chemical strain, *Phys. Rev. B* 80, 064108 (2009).
- [46] M.D. Glinchuk, E.A. Eliseev, A.N. Morozovska, and R. Blinc, Giant magnetoelectric effect induced by intrinsic surface stress in ferroic nanorods, *Phys. Rev. B* 77, 024106 (2008).
- [47] A.N. Morozovska, I.S. Golovina, S.V. Lemishko, A.A. Andriiko, S.A. Khainakov, and E.A. Eliseev, Effect of Vegard strains on the extrinsic size effects in ferroelectric nanoparticles, *Phys. Rev. B* 90, 214103 (2014).
- [48] R. De Wit, *Continual Theory of Disclinations* (Mir, Moscow, 1977) (in Russian).

-
- [49]. A.L. Kolesnikova, R.M. Soroka, and A.E. Romanov, Defects in the elastic continuum: classification, fields and physical analogies, *Materials Physics and Mechanics*. 17, 71 (2013)
- [50]. C. Teodosiu, *Elastic Models of Crystal Defects* (Berlin, Springer-Verlag 1982).
- [51] O. Volnianska and P. Boguslawski, Magnetism of solids resulting from spin polarization of p orbitals, *J. Phys.: Condens. Matter* 22, 073202 (2010).
- [52] H. Jin, Y. Dai, BaiBiao Huang, and M.-H. Whangbo, Ferromagnetism of undoped GaN mediated by through-bond spin polarization between nitrogen dangling bonds, *Appl. Phys. Lett.* 94, 162505(2009)
- [53] Fenggong Wang, Zhiyong Pang, Liang Lin, Shaojie Fang, Ying Dai, and Shenghao Han, Magnetism in undoped MgO studied by density functional theory, *Phys. Rev. B* 80, 144424 (2009).
- [54] J.X. Zhang, Y. L. Li, Y. Wang, Z. K. Liu, L. Q. Chen, Y. H. Chu, F. Zavaliche, and R. Ramesh, Effect of substrate-induced strains on the spontaneous polarization of epitaxial BiFeO₃ thin films, *J. Appl. Phys.* 101, 114105 (2007)
- [55] D. V. Karpinsky, I. O. Troyanchuk, V. Sikolenko, V. Efimov, E. Efimova, M. Willinger, A. N. Salak, and A. L. Kholkin, Phase coexistence in Bi_{1-x}Pr_xFeO₃ ceramics, *J. Mater. Sci.* 49, 6937 (2014).
- [56] J. Silva, A. Reyes, H. Esparza, H. Camacho, and L. Fuentes, BiFeO₃: a review on synthesis, doping and crystal structure, *Integrated Ferroelectrics* 126, 47-59 (2011).
- [57] M. Ramazanoglu, W. Ratcliff, II, Y. J. Choi, Seongsu Lee, S.-W. Cheong, and V. Kiryukhin Temperature-dependent properties of the magnetic order in single-crystal BiFeO₃. *Phys. Rev. B* 83, 174434 (2011)
- [58] M. K. Singh, W. Prellier, M. P. Singh, R. S. Katiyar, and J. F. Scott, Spin-glass transition in single-crystal BiFeO₃, *Phys. Rev. B* 77, 144403 (2008).
- [59] D. Lebeugle, D. Colson, A. Forget, M. Viret, P. Bonville, J. F. Marucco, and S. Fusil, Room-temperature coexistence of large electric polarization and magnetic order in BiFeO₃ single crystals, *Phys. Rev. B* 76, 024116 (2007)
- [60] T.T.A. Lummen, Yijia Gu, Jianjun Wang, Shiming Lei, Fei Xue, Amit Kumar, A.T. Barnes, Eftihia Barnes, Sava Denev, A. Belianinov, M. Holt, A.N. Morozovska, S.V. Kalinin, Long-Qing Chen, and Venkatraman Gopalan, Thermotropic Phase Boundaries in Classic Ferroelectrics, *Nature Communications*, 5, 3172, (2014)
- [61] T. T. A. Lummen, J. Leung, A. Kumar, X. Wu, Y. Ren, B. K. VanLeeuwen, R. C. Haislmaier, M. Holt, K. Lai, S. V. Kalinin, and V. Gopalan, Emergent Low Symmetry Phases and Large Property Enhancements in Ferroelectric KNbO₃ Bulk Crystals, *Adv. Mater.* 29, 1700530 (2017).